Spectroscopic Follow-up of Gaia Exoplanet Candidates: Impostor Binary Stars Invade the Gaia DR3 Astrometric Exoplanet Candidates

Marcus L. Marcussen [ID] and Simon H. Albrecht [ID]
Stellar Astrophysics Centre, Department of Physics and Astronomy, Aarhus University, Ny Munkegade 120, DK-8000 Aarhus C, Denmark; marcus@phys.au.dk

Abstract

In this paper, we report on the follow-up of six potential exoplanets detected with Gaia astrometry and provide an overview of what is currently known about the nature of the entire Gaia astrometric exoplanet candidate sample, 72 systems in total. We discuss the primary false-positive scenario for astrometric planet detections: binary systems with alike components that produce small photocenter motions, mimicking exoplanets. These false positives can be identified as double-lined binaries (SB2) through analysis of high-resolution spectra. Doing so we find that three systems, Gaia DR3 1916454200349735680, Gaia DR3 2052469973468984192, and Gaia DR3 5122670101678217728, are indeed near-equal-mass double-star systems rather than exoplanetary systems. The spectra of the other two analyzed systems, HD 40503 and HIP 66074, are consistent with the exoplanet scenario in that no second set of lines can be found in the time series of publicly available high-resolution spectra. However, their Gaia astrometric solutions imply radial-velocity semiamplitudes $\sim$3 (HD 40503) and $\sim$15 (HIP 66074) larger than what was observed with ground-based spectrographs. The Gaia astrometry orbital solutions and ground-based radial-velocity measurements exhibit inconsistencies in six out of a total of 12 exoplanet candidate systems where such data are available, primarily due to substantial differences between observed ground-based radial-velocity semiamplitudes and those implied by the Gaia orbits. We investigated various hypotheses as to why this might be the case, and although we found no clear perpetrator, we note that a mismatch in orbital inclination offers the most straightforward explanation.

Unified Astronomy Thesaurus concepts: Exoplanet astronomy (486); Astrometric exoplanet detection (2130); Exoplanets (498); Brown dwarfs (185); Astrometry (80); Radial velocity (1332); Binary stars (154); Astrometric binary stars (79); Spectroscopic binary stars (1557)

1. Introduction

The detection of exoplanets through the astrometric reflex motion of their host stars has been predicted to revolutionize the field of exoplanetary science by increasing the total number of known exoplanets by a factor $\sim$4 after the nominal 5 yr mission of Gaia (Gaia Collaboration et al. 2016) and a factor $\sim$14 for the extended 10 yr mission (Perryman et al. 2014). A benefit of the astrometric planet detection method over the radial-velocity (RV) method is that it provides the full orbital solution and the mass of the planet, although obtaining the precision needed for detecting planetary-mass companions is comparatively harder with this method. The astrometric detection sensitivity increases with orbital separation, opposite to the RV and transit methods, which are most suitable for shorter period systems. This makes the methods highly complementary.

On 2022 June 13, the Gaia Data Release 3 (DR3) was published (Gaia Collaboration et al. 2022a). This is the first data release where non-single-star solutions are included. A single Keplarian astrometric orbit model is used. The 169,277 orbital solutions released were compiled from 34 months of Gaia observation (Halbwachs et al. 2022), illustrating the potential of astrometric planet searches. However, the majority of these solutions stem from double-star systems, which produce much larger astrometric signals than those from planetary systems. A small number of the released orbital

solutions (1162) is from the more resource-intensive "exoplanet" pipeline (Holl et al. 2022a) aimed at low signal-to-noise ratio targets with substellar and particularly exoplanetary-mass companions. The inputs for this exoplanet pipeline either were targets where the two-body orbit model of the "binary" pipeline (Gaia Collaboration et al. 2022b) did not improve enough the single star fit (the `orbitalAlternative` solutions) or were preselected targets (`orbitalTargetedSearch`). Many of the preselected targets were chosen because they were known to harbor planets or brown dwarfs beforehand. In total 1843 astrometric brown dwarf and 72 exoplanet candidates were published in DR3 (Gaia Collaboration et al. 2022b).

An overview of all 102 systems with astrometric signals small enough to naively imply a companion mass $<20M_{\rm Jup}$ is shown in Figure 1 in a color–magnitude diagram. In order to get a sense of the prevalence of binary systems to exoplanetary systems, the figure includes 30 systems that are not among the 72 released exoplanet candidates,[1] due to their high likelihood of being binaries. For the masses of the primary stars, we used the m_1 masses from the binary_masses table where available. For a few systems where these were not available, we used the single-source mass_flame from the astrophysical_parameters table. The systems are colored according to the current status of their nature, also available in Table 1. A subset of the systems in this table have already been studied for consistency between the astrometric and RV data by Holl et al. (Holl 2022a), Gaia Collaboration et al. (2022b), and Winn (2022). We discuss their results in the sections of the specific systems. In Figure 2, we show for these same systems the companion mass estimates,

---

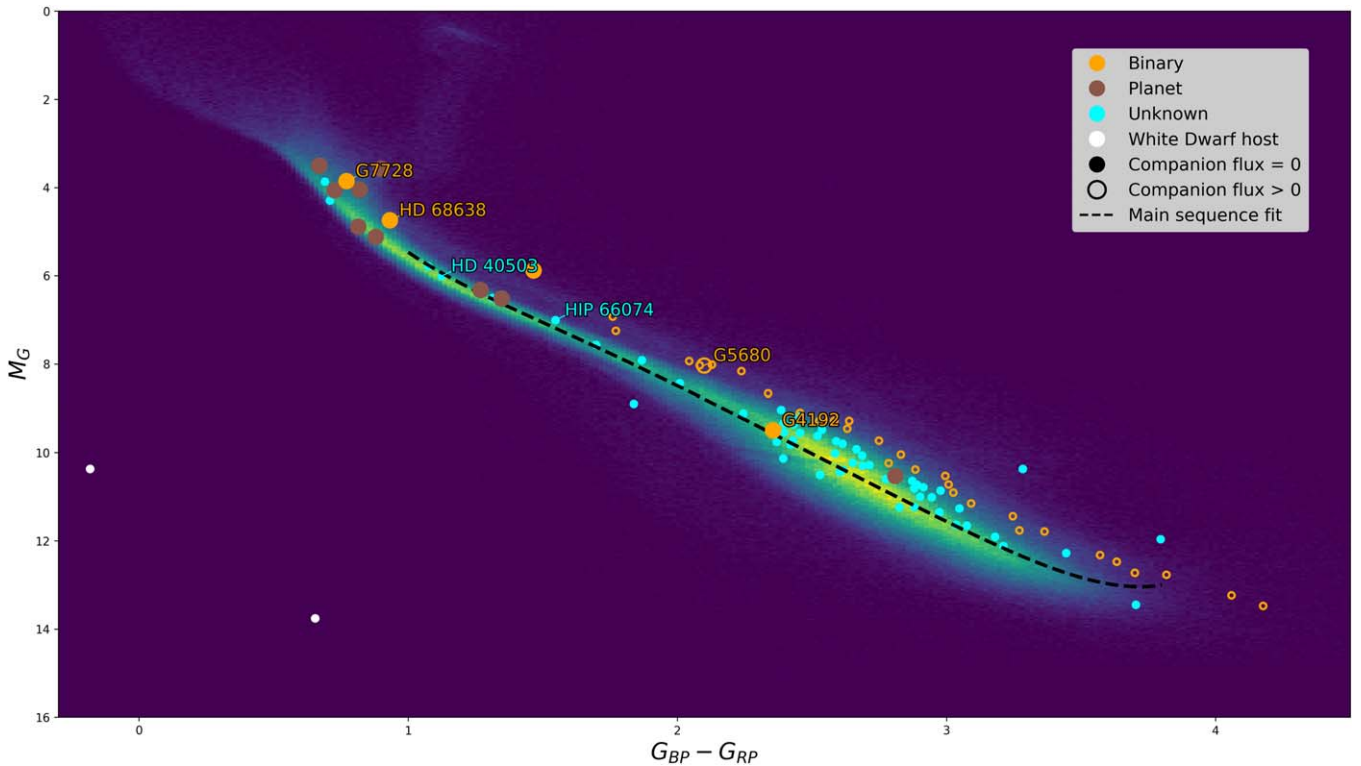[1] https://www.cosmos.esa.int/web/gaia/exoplanets

Figure 1. Astrometric exoplanet candidate systems in an H-R diagram. All Gaia DR3 systems where the astrometric two-body motion of the source is small enough to indicate a companion with a mass $<20M_{\rm Jup}$, assuming the companion does not contribute any flux, are shown here as circles. The released Gaia astrometric exoplanet candidates are shown using closed circles while open circles indicate systems where a lower bound on the flux of the companion is nonzero as per the `binary_masses` table. Large circles indicate systems where the nature of the companion is confirmed, either here or in the literature; see also Table 1. The systems are colored according to the current knowledge of the nature of the companion, where brown indicates a planetary companion, orange indicates a stellar companion, and cyan indicates that it is unknown. The two white dots indicate two white dwarf hosts where the companion nature is unknown. The comparison stars shown in the background are the 1,000,000 nearest-to-us Gaia DR3 stars whose estimated parallax is more than 10 times its uncertainty. The density of these stars is represented as a purple-to-yellow heatmap, where purple (yellow) indicates a low (high) density. Since most of the planet candidates are too faint to have Gaia DR3 reddening and extinction parameters, candidates and comparison stars alike are shown using their uncorrected colors and magnitudes. The black dashed line represents the best fit to the main sequence. The six systems discussed in detail in Section 4 are indicated by their name.

apparent magnitudes, and the relative uncertainty of their astrometric orbits. We note that only 17 of the systems have companion mass estimates below the often-used limit of $13M_{\rm Jup}$ between planets and brown dwarf.

With only one previous discovery (Curiel et al. 2022), astrometry is not yet a well-developed technique for the detection of exoplanets. The method comes with its own set of unique challenges. In particular, the photocenter (the apparent position of the objects) motion of a binary system can be arbitrarily small, and thereby mimic a low-mass companion, as the flux ratio of the two stars approaches their mass ratio. In order for Gaia to achieve its full planet detection potential, we need to understand better the nature of these challenges and their prevalence, and we need to provide paths to overcome them. In this work, we discuss possible steps to confirm or reject the planet status of an astrometric candidate system using high-resolution spectra. Specifically, we are employing both publicly available spectra (of the three potentially new astrometric exoplanet discoveries discussed in Holl et al. 2022a; Gaia Collaboration et al. 2022b) as well as new FIES spectra (of another three exoplanet candidates) that we obtained from the Nordic Optical Telescope (NOT).[2]

Our paper is structured as follows: We first summarize important aspects of astrometric binary signals in Section 2, and we discuss how to differentiate between genuine planet detections and false positives in Section 3. In Section 4, we analyze six exoplanet candidate systems, and we discuss our findings in Section 5.

2. Astrometric Signal

A star and its companion orbit their common barycenter. If the companion is an exoplanet, i.e., dark and low mass, the observed astrometric reflex motion of the source is small and coincides with the motion of the star. If the companion is another star, though, i.e., it has a higher mass and contributes flux, the actual motion of the primary star is then larger, but the photocenter of the system is located between the two components. Its astrometric amplitude is smaller than the actual motion of the primary star and can be arbitrarily small given the system parameters. In this section, we outline how the observed semimajor axis relates to the flux and mass ratios of the components in systems where the primary component has a single companion (Section 2.1) and in systems where an inner pair of stars orbits an outer companion (Section 2.2).

The total astrometric motion of a star orbited by a single companion is the linear combination of the 5 parameter single-source astrometric model and a Keplarian 7 parameter model.

---

[2] These spectra have been obtained through the *Fast-Track* channel available at the observatory; http://www.not.iac.es/observing/proposals/.

Table 1
Apparent Low-mass Companions

Gaia DR3 ID	Name	Solution Type	Status	RV Data	M_1 ($M_\odot$)	M_2 (M_J)	Flux Ratio F_2/F_1	G_{Mag}	Distance (pc)	References
1035000055055287680	HD 68638	OTSV	SB2	Consistent	[1]$0.95^{+1.00}_{-0.82}$	31^{+48}_{-14}	~1	7.3	32.5	1, 2, 3
2884087104955208064	HD 40503	OTSV	Unknown	Inconsistent	[1]$0.79^{+0.85}_{-0.57}$	5^{+8}_{-3}	[0–1]	9.0	39.2	2, 3
1712614124767394816	HIP 66074	OTSV	Unknown	Inconsistent	[1]$0.71^{+0.76}_{-0.51}$	7^{+11}_{-3}	[0–1]	9.7	35.4	2, 3, 4, 5
1916454200349735680		Orbital	SB2	Consistent	[1]$0.63^{+0.68}_{-0.48}$	17^{+26}_{-8}	~0.88	10.9	37.1	This work
2052469973468984192		Orbital	SB2	Consistent	[1]$0.47^{+0.52}_{-0.29}$	18^{+27}_{-9}	~0.85	10.7	17.4	This work
5122670101678217728	HD 12357	Orbital	SB2	Consistent	[1]$1.04^{+1.10}_{-0.97}$	21^{+33}_{-10}	~1	8.9	102.8	This work
4062446910648807168	HR 164604	OTSV	Exoplanet	No	[2]$0.75^{+0.79}_{-0.71}$	14^{+24}_{-5}	~0	9.3	40.0	6
1594127865540229888	HD 132406	OTSV	Exoplanet	Inconsistent	[2]$0.97^{+1.01}_{-0.93}$	6^{+11}_{-3}	~0	8.3	70.5	4, 7
2367734656180397952	BD-17 63	OTSV	Exoplanet	Consistent	[1]$0.74^{+0.79}_{-0.56}$	4^{+7}_{-2}	~0	9.2	34.5	4, 8
4745373133284418816	HR 810	OTS	Exoplanet	Inconsistent	[1]$1.09^{+1.15}_{-0.93}$	6^{+10}_{-3}	~0	5.3	17.4	4, 5, 9, 10, 11
6373290674775530368	HD 81040	OTSV	Exoplanet	Consistent	[1]$0.98^{+1.03}_{-0.68}$	8^{+12}_{-4}	~0	7.6	34.4	4, 12
4901802507993393664	HD 3221	OTS	SB2	No	[3]1	14	~1	9.1	44.4	13
5855730584310531200	HD 111232	OTSV	Exoplanet	Inconsistent	[1]$0.93^{+0.99}_{-0.68}$	8^{+13}_{-4}	~0	7.4	28.9	4, 14, 15, 9
2603090003484152064	GJ 876	OTSV	Exoplanet	No	[1]$0.38^{+0.43}$	4^{+5}_{-2}	~0	8.9	4.7	16
4976894960284258048	HD 142	OTS	Exoplanet	No	[1]$1.19^{+1.25}_{-1.06}$	7^{+11}_{-3}	~0	5.6	26.2	17
6421118739093252224	HD 175167	OTSV	Exoplanet	Inconsistent	[2]$1.09^{+1.13}_{-1.05}$	10^{+16}_{-5}	~0	7.8	71.2	4, 6
4764340705296117120		Orbital	Unknown	No	[1]$0.34^{+0.39}_{-0.18}$	13^{+19}_{-6}	[0–1]	14.8	61.8	
1984587671751337600		Orbital	Unknown	No	[1]$0.36^{+0.41}_{-0.24}$	19^{+29}_{-9}	[0.34–1]	14.2	54.0	
4392798821280870912		Orbital	Unknown	No	[1]$0.42^{+0.47}_{-0.26}$	15^{+23}_{-7}	[0.05–1]	13.4	42.6	
5220375041387610880		Orbital	Unknown	No	[1]$0.74^{+0.79}_{-0.53}$	20^{+31}_{-9}	[0–1]	12.8	183.6	
6418925831870553472		Orbital	Unknown	No	[1]$0.37^{+0.42}_{-0.20}$	15^{+23}_{-8}	[0–1]	15.0	84.0	
2571855077162098944		Orbital	Unknown	No	[1]$0.54^{+0.59}_{-0.37}$	15^{+23}_{-7}	[0–1]	14.5	114.6	
5036787935627755520		Orbital	Unknown	No	[1]$0.22^{+0.26}_{-0.10}$	12^{+17}_{-6}	[0.21–1]	14.9	33.5	
932447162423519232		ASSB1	Unknown	No	[1]$0.63^{+0.68}_{-0.48}$	17^{+27}_{-8}	[0.22–1]	11.6	52.5	
5654515588409756160		Orbital	Unknown	No	[1]$0.26^{+0.31}_{-0.12}$	23^{+34}_{-11}	[0–1]	16.4	88.4	
5271515801094390912		Orbital	Unknown	No	[1]$0.56^{+0.61}_{-0.39}$	21^{+32}_{-10}	[0–1]	12.2	55.6	
5085864568417061120		Orbital	Unknown	No	[1]$0.46^{+0.51}_{-0.28}$	16^{+24}_{-8}	[0–1]	13.7	55.8	
4232979927866697088		Orbital	Unknown	No	[1]$0.41^{+0.46}_{-0.24}$	21^{+32}_{-10}	[0–1]	14.8	79.2	
2845310284780420864		Orbital	Unknown	No	[1]$0.37^{+0.42}_{-0.20}$	10^{+15}_{-5}	[0–1]	13.8	41.5	
4188996885011268608		Orbital	Unknown	No	[1]$0.23^{+0.28}_{-0.09}$	8^{+12}_{-4}	[0–1]	13.5	17.8	
4842246017566495232		Orbital	Unknown	No	[1]$0.36^{+0.41}_{-0.19}$	8^{+12}_{-4}	[0–1]	13.0	31.9	
1336053176328998144		Orbital	Unknown	No	[1]$0.44^{+0.49}_{-0.33}$	19^{+29}_{-9}	[0.48–1]	14.3	83.2	
6081071334868194176		Orbital	Unknown	No	[1]$0.61^{+0.66}_{-0.43}$	20^{+31}_{-10}	[0–1]	12.9	99.0	
405316961377489792		Orbital	Unknown	No	[1]$0.27^{+0.32}_{-0.13}$	22^{+33}_{-10}	[0–1]	15.7	77.4	
6671454584430500864		Orbital	Unknown	No	[1]$0.57^{+0.62}_{-0.43}$	14^{+24}_{-6}	[0.17–1]	13.9	112.4	
3621891774065137408		Orbital	Unknown	No	[1]$0.36^{+0.41}_{-0.22}$	19^{+29}_{-9}	[0.19–1]	15.5	92.3	
4159075462792179456		Orbital	Unknown	No	[1]$0.35^{+0.40}_{-0.20}$	8^{+13}_{-4}	[0.07–1]	14.9	64.4	
3665298981300771200		Orbital	Unknown	No	[1]$0.69^{+0.74}_{-0.54}$	20^{+31}_{-9}	[0.29–1]	10.7	48.7	
4810127839810808576		Orbital	Unknown	No	[1]$0.55^{+0.60}_{-0.38}$	16^{+24}_{-7}	[0.07–1]	13.0	61.4	
2998643469106143104		Orbital	Unknown	No	[1]$0.37^{+0.41}_{-0.20}$	20^{+30}_{-10}	[0–1]	14.0	48.3	
557717892980808960		Orbital	Unknown	No	[1]$0.55^{+0.60}_{-0.37}$	8^{+13}_{-4}	[0–1]	12.0	40.0	
6381440834777420928		Orbital	Unknown	No	[1]$0.28^{+0.33}_{-0.13}$	21^{+32}_{-10}	[0–1]	15.1	60.6	
4596564611107874944		Orbital	Unknown	No	[1]$0.32^{+0.37}_{-0.17}$	19^{+29}_{-9}	[0.10–1]	14.8	54.9	
2271703211828512896		Orbital	Unknown	No	[1]$0.16^{+0.21}_{-0.07}$	13^{+20}_{-6}	[0.30–1]	16.4	42.3	
5612039087715504640		Orbital	Unknown	No	[1]$0.28^{+0.33}_{-0.13}$	14^{+21}_{-7}	[0–1]	13.9	32.4	
834357565445682944		Orbital	Unknown	No	[1]$0.43^{+0.48}_{-0.25}$	17^{+25}_{-8}	[0–1]	13.7	53.6	
5446516751833167744		Orbital	Unknown	No	[1]$0.27^{+0.32}_{-0.12}$	17^{+25}_{-8}	[0.01–1]	16.0	70.4	
846058258950880384		Orbital	Unknown	No	[1]$0.60^{+0.65}_{-0.49}$	15^{+24}_{-7}	[0.44–1]	13.9	143.4	
2117364283603705984		Orbital	Unknown	No	[1]$0.41^{+0.46}_{-0.29}$	15^{+23}_{-7}	[0.37–1]	13.5	48.9	
2074815898041643520		Orbital	Unknown	No	[1]$0.36^{+0.41}_{-0.20}$	21^{+32}_{-10}	[0–1]	13.2	41.3	
2047188847334279424		OTS	Unknown	No	[1]$0.96^{+1.01}_{-0.82}$	14^{+22}_{-7}	[0–1]	7.3	32.6	
6685861691447769600		Orbital	Unknown	No	[1]$0.50^{+0.55}_{-0.32}$	20^{+31}_{-10}	[0–1]	14.3	99.6	
6079316686107743488		Orbital	Unknown	No	[1]$0.38^{+0.43}_{-0.20}$	20^{+31}_{-10}	[0–1]	14.7	66.4	
4308923357759527424		Orbital	Unknown	No	[1]$0.19^{+0.24}_{-0.08}$	7^{+11}_{-3}	[0.15–1]	15.6	38.1	
1298992006611690112		Orbital	Unknown	No	[1]$0.52^{+0.57}_{-0.36}$	14^{+21}_{-7}	[0.11–1]	13.6	73.9	
1878822452815621120		OTS	Unknown	No	[1]$0.82^{+0.88}_{-0.61}$	16^{+25}_{-8}	[0–1]	9.8	62.3	
1879554280883275136		Orbital	Unknown	No	[1]$0.43^{+0.48}_{-0.26}$	18^{+27}_{-9}	[0–1]	14.3	79.3	
6471102606408911360		Orbital	Unknown	No	[1]$0.65^{+0.81}_{-0.49}$	23^{+36}_{-11}	[0–1]	14.3	62.1	

Table 1
(Continued)

Gaia DR3 ID	Name	Solution Type	Status	RV Data	M_1 $(M_\odot)$	M_2 (M_J)	Flux Ratio F_2/F_1	G_{Mag}	Distance (pc)	References
5671384265738137984		Orbital	Unknown	No	[1]$0.15^{+0.20}_{-0.07}$	16^{+24}_{-8}	[0.27–1]	15.7	28.3	
2104920835634141696		Orbital	Unknown	No	[1]$0.21^{+0.26}_{-0.08}$	13^{+19}_{-6}	[0–1]	15.4	46.2	
373892712892466048		Orbital	Unknown	No	[1]$0.51^{+0.56}_{-0.33}$	17^{+25}_{-8}	[0–1]	13.9	75.3	
5399010462168339456		Orbital	Unknown	No	[1]$0.47^{+0.52}_{-0.39}$	14^{+22}_{-6}	[0.65–1]	13.8	79.6	
5618776310850226432		Orbital	Unknown	No	[1]$0.47^{+0.52}_{-0.29}$	21^{+32}_{-10}	[0–1]	14.7	94.1	
6781298098147816192		Orbital	Unknown	No	[1]$0.32^{+0.37}_{-0.16}$	6^{+10}_{-3}	[0–1]	14.4	48.1	
2050702366781291776		Orbital	Unknown	No	[1]$0.26^{+0.31}_{-0.13}$	18^{+27}_{-9}	[0.22–1]	16.4	85.2	
1052042828882790016		Orbital	Unknown	No	[1]$0.47^{+0.52}_{-0.30}$	21^{+32}_{-10}	[0–1]	14.0	78.1	
726588585356221568		Orbital	Unknown	No	[1]$0.27^{+0.32}_{-0.15}$	20^{+30}_{-9}	[0.28–1]	15.6	67.8	
5486916932205092352		Orbital	Unknown	No	[1]$0.33^{+0.38}_{-0.17}$	11^{+16}_{-6}	[0–1]	12.2	17.1	
5052449001298518528		Orbital	Unknown	No	[1]$0.47^{+0.52}_{-0.29}$	20^{+31}_{-10}	[0–1]	13.6	59.2	
246890014559489792		Orbital	Unknown	No	[1]$0.36^{+0.41}_{-0.19}$	6^{+9}_{-3}	[0–1]	14.4	52.5	
5055723587443420928		Orbital	Unknown	No	[1]$0.45^{+0.50}_{-0.27}$	19^{+30}_{-9}	[0–1]	14.6	137.7	
3676303512147120512		Orbital	Unknown	No	[1]$0.23^{+0.28}_{-0.10}$	18^{+27}_{-9}	[0–1]	14.8	38.7	
1059462676944293376		Orbital	Unknown	No	[1]$0.48^{+0.53}_{-0.35}$	16^{+24}_{-8}	[0.33–1]	14.7	111.6	
5490183684330661504		Orbital	Unknown	No	[1]$0.14^{+0.19}_{-0.05}$	23^{+36}_{-11}	[0–1]	17.7	72.4	
2277249663873880576		Orbital	Unknown	No	[1]$0.50^{+0.55}_{-0.32}$	11^{+17}_{-5}	[0–1]	12.9	51.1	
2259699048817216256		Orbital	Unknown	No	[1]$0.62^{+0.67}_{-0.49}$	16^{+24}_{-7}	[0.31–1]	13.1	105.9	
2259968811419624448		Orbital	Unknown	No	[1]$0.40^{+0.45}_{-0.23}$	22^{+33}_{-10}	[0–1]	13.9	54.9	
4812716639938468992		Orbital	Unknown	No	[1]$0.31^{+0.36}_{-0.15}$	22^{+33}_{-11}	[0–1]	14.7	48.2	
6521749994635476992		Orbital	Unknown	No	[1]$0.48^{+0.53}_{-0.30}$	15^{+22}_{-7}	[0–1]	13.6	62.4	
1457486023639239296		Orbital	Unknown	No	[1]$0.64^{+0.69}_{-0.45}$	13^{+21}_{-6}	[0–1]	11.9	73.8	
1462767459023424512		Orbital	Unknown	No	[1]$0.37^{+0.41}_{-0.19}$	8^{+12}_{-4}	[0–1]	15.1	72.0	
73648110622521600		Orbital	Unknown	No	[1]$0.25^{+0.30}_{-0.11}$	20^{+30}_{-10}	[0–1]	15.5	58.6	
5796338299045711232		Orbital	Unknown	No	[1]$0.18^{+0.23}_{-0.08}$	11^{+17}_{-5}	[0.37–1]	14.8	25.8	
3937630969071148032		Orbital	Unknown	No	[1]$0.43^{+0.48}_{-0.26}$	20^{+30}_{-10}	[0–1]	14.7	84.7	
2446599193562312320		Orbital	Unknown	No	[1]$0.50^{+0.55}_{-0.33}$	24^{+37}_{-11}	[0–1]	14.7	129.1	
1862136504889464192		Orbital	Unknown	No	[1]$0.37^{+0.42}_{-0.21}$	16^{+23}_{-8}	[0–1]	15.2	83.1	
3925216795598987264		Orbital	Unknown	No	[1]$0.40^{+0.45}_{-0.25}$	19^{+29}_{-9}	[0.16–1]	14.8	75.0	
2824801747222539648		Orbital	Unknown	No	[1]$0.44^{+0.49}_{-0.27}$	19^{+29}_{-9}	[0–1]	14.0	70.4	
6694115931396057728		Orbital	Unknown	No	[1]$0.33^{+0.38}_{-0.17}$	9^{+14}_{-5}	[0–1]	13.4	38.1	
4698424845771339520		OTS	Unknown	No	[1]$0.65^{+0.81}_{-0.49}$	9^{+14}_{-4}	[0–1]	13.7	9.7	
4702845638429469056		Orbital	Unknown	No	[1]$0.43^{+0.47}_{-0.26}$	7^{+10}_{-3}	[0–1]	13.9	68.2	
6677563745912843776		Orbital	Unknown	No	[1]$0.39^{+0.44}_{-0.21}$	23^{+35}_{-11}	[0–1]	15.5	94.7	
6354671987249126784		ASSB1	Unknown	No	[1]$0.69^{+0.75}_{-0.64}$	13^{+21}_{-6}	[0.12–1]	9.5	32.5	
522135261462534528		OTS	Unknown	No	[1]$1.09^{+1.15}_{-0.79}$	7^{+11}_{-3}	[0–1]	6.4	27.0	
5375875638010549376		Orbital	Unknown	No	[1]$0.40^{+0.45}_{-0.23}$	14^{+21}_{-6}	[0–1]	14.4	67.1	
1610837178107032192		OTS	Unknown	No	[1]$1.13^{+1.19}_{-0.97}$	13^{+21}_{-6}	[0–1]	8.2	73.7	
4963614887043956096		OTS	Unknown	No	[3]1	46	[0–1]	15.0	40.2	
3120450116011961984		Orbital	Unknown	No	[1]$0.64^{+0.69}_{-0.49}$	16^{+25}_{-8}	[0.21–1]	12.8	94.7	
4983571882081864960		Orbital	Unknown	No	[1]$0.47^{+0.52}_{-0.29}$	12^{+19}_{-6}	[0–1]	13.3	55.5	
5236626338671861760		Orbital	Unknown	No	[3]1	21	[0–1]	13.9	51.3	
5437488554482255872		Orbital	Unknown	No	[1]$0.50^{+0.55}_{-0.37}$	18^{+27}_{-8}	[0.29–1]	13.4	67.4	
198464052134353536		Orbital	Unknown	No	[1]$0.20^{+0.25}_{-0.09}$	11^{+17}_{-5}	[0.22–1]	14.4	24.1	

Note. The 102 listed systems are the union of the following subsets: (A) the released Gaia exoplanet candidates and (B) all systems whose Gaia nss_two_body_orbit implies $M_2 < 20 M_J$ assuming a dark companion, regardless of the binary_masses flux ratio value. The same systems are shown in Figure 1 and Figure 2. The source of information for the mass of the primary component M_1 and its uncertainty was in order of decreasing priority: M_1 from binary_masses, "mass_flame" from astrophysical_parameters, and $M_1 = 1 M_\odot$, denoted by 1, 2, and 3 respectively in the corresponding column of the table. The top six systems of the table are those analyzed in this paper. The system name column shows the systems previously studied in the literature. Whether RV data from ground-based spectroscopy is available for a system, and if so, whether it is consistent with the nss_two_body_orbit solution and companion mass or not is listed in the "RV data" column. We define the data sets to be consistent if all the orbital parameters as well as the RV semiamplitudes are within 3σ of one another. However, for our three systems with only two spectra each, only the orbital period and RV semiamplitudes are tested for consistency. The distance column is 1/parallax, where the parallax is from the gaia_source table. The solution type column refers to the nss_solution_type of the nss_two_body_orbit table, and OTS and OTSV refer to orbitalTargetedSearch and OrbitalTargetedSearchValidated, respectively. References: (1) Busà et al. (2007); (2) Holl et al. (2022a); (3) Gaia Collaboration et al. (2022b); (4) Winn (2022); (5) Butler et al. (2017); (6) Arriagada et al. (2010); (7) da Silva et al. (2007); (8) Moutou et al. (2009); (9) Trifonov et al. (2020); (10) Kürster et al. (2000); (11) Naef et al. (2001); (12) Sozzetti et al. (2006); (13) Bonavita et al. (2022); (14) Minniti et al. (2009); (15) Mayor et al. (2004); (16) Marcy et al. (2001); (17) Wittenmyer et al. (2012).

The single-source model consists of the two position parameters R.A. and decl., the proper motions, $\mu_{R.A.}$ and $\mu_{decl.}$, and the parallax, ϖ. The Keplarian model consists of the orbital period P, time of perisastron passage T_0, eccentricity e, semimajor axis of the star's orbit a_1, the orbital inclination i, the argument of periastron ω, and the R.A. of the ascending node Ω. The latter four parameters are the Campbell elements that may also be expressed by the Thiele Innes coefficients A, B, F, G. For more information on the Thiele Innes coefficients and how they are derived from the Gaia along-scan measurements, see Gaia Collaboration et al. (2022b).

2.1. Binary Systems

For systems with a single companion, the semimajor axis of the relative orbit a is the sum of the semimajor axes a_1 and a_2 around the barycenter of the star and companion respectively; see Figure 3. The ratio of the semimajor axes is equal to the inverse ratio of the masses, $M_2/M_1 = a_1/a_2 \equiv q$, giving

$$a_1 = a\frac{M_2}{M_2 + M_1} = a\frac{q}{q + 1}. \tag{1}$$

However, in completely unresolved systems where the secondary component has a nonnegligible flux, we observe the motion of a system's photocenter, i.e., the flux-weighted mean position of the two components. This gives the following definition for the semimajor axis of the photocenter a_0:

$$a_0 = \left| \frac{F_1 a_1 - F_2 a_2}{F_1 + F_2} \right|. \tag{2}$$

Here, F_i indicates the flux of the ith component (in the bandpass in which the astrometric signal is measured). Trivially, the astrometric observable, a_0, is equal to a_1 when the companion is dark ($F_2 = 0$). This scenario is illustrated in the left panel of Figure 3. A ratio of the fluxes of $\epsilon \equiv F_2/F_1$ equal to 1 leads to $a_0 = (a_1 - a_2)/2$. If q is also 1, then the photocenter remains in the barycenter of the system. In the case that F_2 is nonzero, the semimajor axis of the photocenter is given by the following:

$$
\begin{aligned}
a_0 &= \left| \frac{F_1 a_1 - F_2 a_2}{F_1 + F_2} \right| = \left| \frac{a_1 - \epsilon a_2}{1 + \epsilon} \right| \\
&= \left| \frac{a - a_2 - \epsilon a_2}{1 + \epsilon} \right| \\
&= \left| \frac{a}{1 + \epsilon}\left(1 - \frac{1}{1 + q}(1 + \epsilon)\right) \right| \\
&= \left| a\left(\frac{1}{1 + \epsilon} - \frac{1}{1 + q}\right) \right|.
\end{aligned} \tag{3}
$$

Making use of Kepler's third law we find the following:

$$a_0^3 = \left| GM_1\left(\frac{P}{2\pi}\right)^2(1 + q)\left(\frac{1}{1 + q} - \frac{1}{1 + \epsilon}\right)^3 \right|. \tag{4}$$

The gravitational constant is indicated by G. A tiny photocenter movement may thus originate from two common but astrometrically indistinguishable scenarios: (I) a single star orbited by a dark, low-mass companion or (II) a double-star system with $\epsilon \approx q$, illustrated in the left and middle panels of Figure 3 respectively. Therefore, in order to confirm an astrometric exoplanet candidate detected by the small

astrometric reflex motion of its host star, additional measurements using different methods are needed.

We note that if q exceeds ϵ, the location of the photocenter is between the barycenter and the secondary component rather than the primary. This will result in a $180°$ phase-shift in ω of the photocenter orbit. With RV measurements of the primary component, one would in principle be able to distinguish between $q > \epsilon$ and $q < \epsilon$ by the opposing sign of the RV signal to that inferred by the astrometric photocenter motion. However, because the astrometric motion is the sky-projection of the three-dimensional orbit, one cannot a priori distinguish between the configurations (Ω, ω) and $(\Omega + 180°, \omega + 180°)$. Even though we can resolve this ambiguity of the photocenter orbital configuration by combining RV data with an astrometric solution, we thus still face uncertainty about whether the orbit corresponds to the orbit of the primary or secondary component of the system. In other words, if the RV signal's sign contradicts our expectations from the photocenter orbit, it remains unclear whether this discrepancy arises from an incorrect assumption about ω or from a larger value of q compared to ϵ. In order to truly lift this degeneracy, second order effects like the light-travel time (light has a shorter travel distance when the component is on "our side" of the sky-plane) and local perspective effects (the parallax is larger when the component is on "our side" of the sky-plane) would need to be taken into account (Halbwachs 2009). These effects are not modeled in Gaia DR3. If we do not know whether the photocenter orbit traces out the orbit of the secondary or primary, i.e., if q is larger or smaller than ϵ, and if we have no prior on the flux ratio of the components, i.e., ϵ is anywhere between 0 and 1, the knowledge of a_0 alone is not enough to determine M_2.

2.2. Triple Systems

Another configuration that could conceivably produce a small photocenter semimajor axis, a_0, is a hierarchical triple star system where a large amplitude astrometric signal from a double-star system is muted by the presence of a brighter third component farther away. If the distance to the third component is sufficiently large (but not so large as to be resolvable), its long-term contribution to the astrometry would be undetectable in the Gaia data, but the amplitude of a_0 would be diminished by a factor

$$(F_1 + F_2)/F_3. \tag{5}$$

Here, F_3 denotes the flux of the third star in the relevant bandpass. This is illustrated in the right-hand panel of Figure 3. The third component might also be a nonassociated source, i.e., a chance alignment.

3. Differentiating between Stellar and Planetary Companions

In this section, we describe ways to determine the nature of a companion given the detection of an astrometric Keplarian signal with a small photocenter.

3.1. Color–Magnitude Relation

The luminosity of a star on the main sequence can be well constrained by its effective temperature. A system of two identical, unresolved stars has twice the luminosity of a similar single star but the same effective temperature, in turn elevating
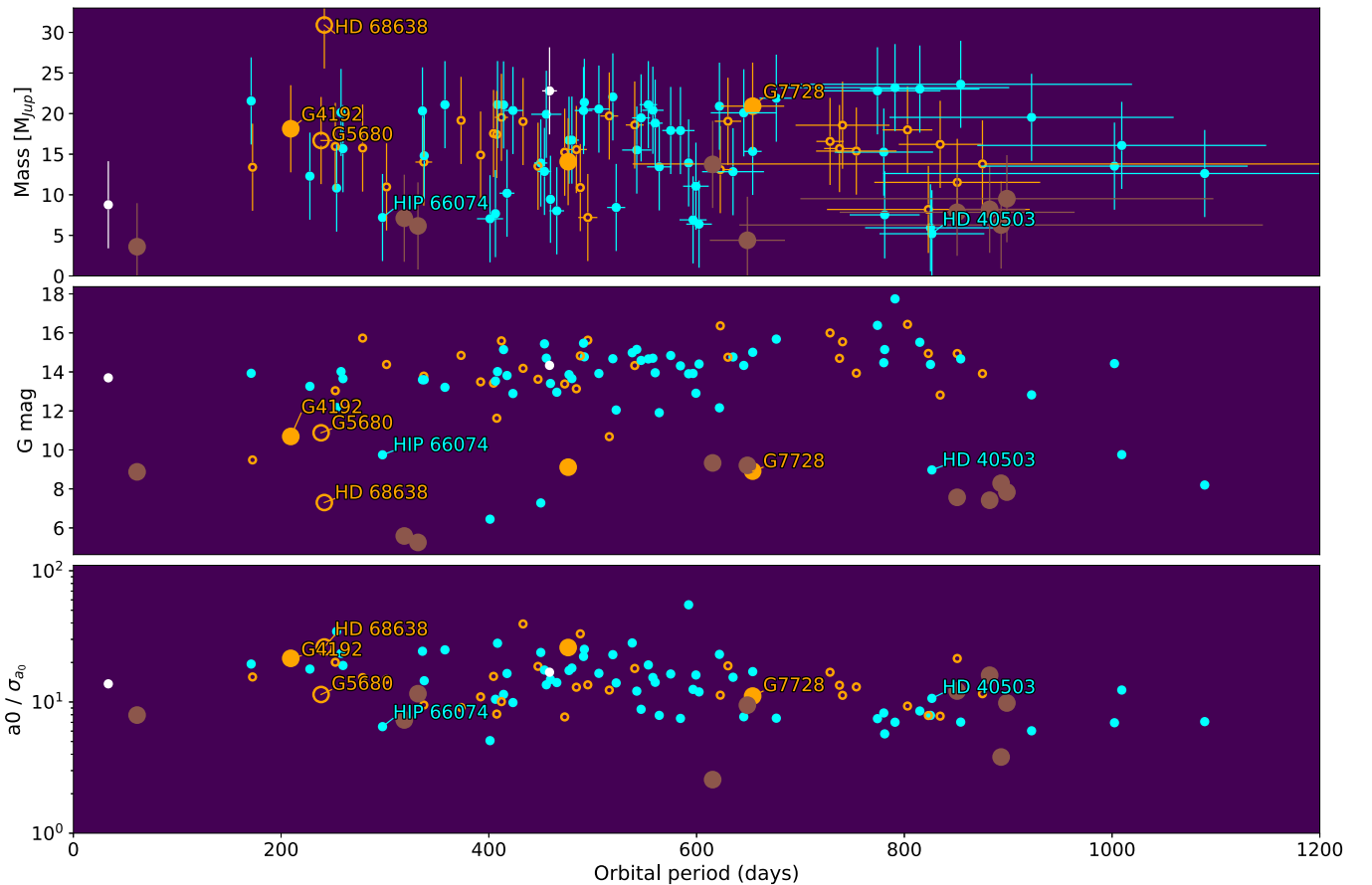
Figure 2. Exoplanet candidate parameters. Top panel: companion masses of the same sample as shown in Figure 1 are calculated under the assumption that their flux contribution is negligible compared to their host and assuming Gaussian uncertainties in photocenter semimajor axis a0, orbital period P, and primary mass M_1. Middle panel: the G magnitudes of the sample. Bottom panel: the size of the photocenter semimajor axis relative to its uncertainty, which can be taken as a proxy for the robustness of the Keplarian orbit detection.

its position relative to the single star main sequence in an H-R diagram. This fact allows for an estimate of the flux ratio F_1/F_2 using isochrones (Gaia Collaboration et al. 2022b) giving a first indication of whether an astrometric two-body orbit is caused by a stellar or substellar companion. In Figure 1, we can observe how all the systems, whose flux ratio have been estimated to be nonzero this way (indicated by open circles), are located clearly above the single star main sequence, i.e., their luminosity is higher than expected, given its observed color, if the system were a single star. For DR3 systems with both astrometric and spectroscopic solutions, first M_2 is derived from the RV semiamplitude, K, via Equation (3) in Gaia Collaboration et al. (2022b), and then the flux ratio is inferred from how much smaller the astrometric signal is (our Equation (3)). The masses shown in Figure 2 are all calculated using Equation (4) from the astrometric semimajor axis alone, i.e., using $F_2 = 0$ for all systems. We do this in order to get a better sense of the ratio of stellar companions to substellar companions among all orbital solutions with small a_0.

3.2. Spectra

High-resolution spectroscopic follow-up observations can be used to reveal the impostor binaries among the astrometric exoplanet candidate systems. Spectra from star–planet systems are fundamentally different from those from star–star systems: only one set of absorption lines is present, and the RV of the host star is much smaller due to the lower mass of the

companion. This means the Doppler-shift of the spectrum over time is much smaller. Depending on whether an impostor binary system consists of two truly identical twins (i.e., have very similar effective temperatures, luminosities, rotation speeds, and masses) or whether the stars are significantly different where q happens to be close to ϵ (e.g., a red giant and a main-sequence star), the two sets of oppositely shifting absorption lines produced by the binary system may present themselves differently:

Uneven twin impostors. If one of the components is of a very different stellar class and/or has a very different rotation rate, the absorption lines from a single component may dominate the spectrum of the system. Such a system would be classified as a single-lined binary (SB1) system. Impostors of this type allow us to measure the orbital RV semiamplitude of the component most visible in the spectra, which will be significantly larger than if it were an exoplanetary system. If an astrometric exoplanet candidate is in fact an SB1 binary, a few observations at different orbital phases are enough to identify it as such. If the orbital period and time of periastron passage are well determined from the astrometry such that the follow-up observations are ensured to be undertaken at advantageous points of the orbit, just two observations may be enough.

Identical twin impostors. If, on the other hand, the two stars are very alike in every way, their absorption lines will be similar in shape and size. Additionally, the RV shift of each star's absorption lines will be equal in amplitude but with
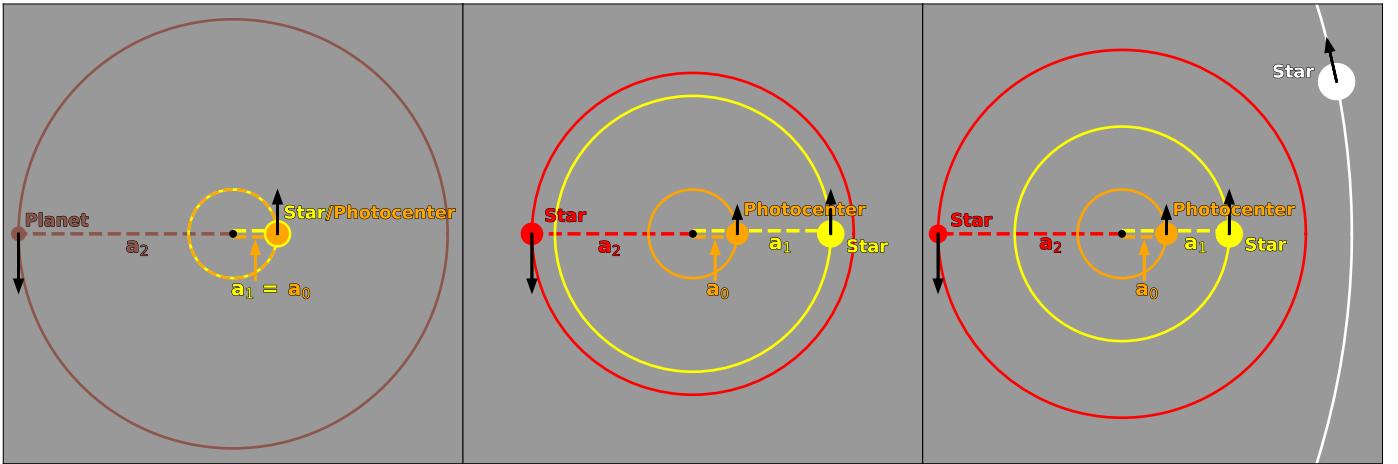
Figure 3. Photocenter. Not-to-scale illustration of three different geometries of face-on, circular orbits that the same astrometric signal may originate from. Left panel: an exoplanet orbiting a star. The semimajor axis of the exoplanet orbit, a_2, is much larger than the orbit of the star, a_1, due to the large difference in mass. The flux contribution from the planet is negligible, and thus the photocenter closely follows the star. Middle panel: twin stars (i.e., almost equal flux and mass stars) orbit their barycenter (black dot). The primary component, the yellow star, is slightly more massive than the secondary component, the red star, leading to a smaller semimajor axis a_1 than a_2. The ratio of the masses is slightly higher than the ratio of the received fluxes, $M_2/M_1 > F_2/F_1$, resulting in a small photocenter semimajor axis a_0 that traces out (a diminished version of) the orbit of the primary component. Right panel: two stars with significantly different masses and fluxes in a hierarchical triple system, where the center-of-mass of the red and yellow star orbits around a larger and brighter third component that is very far away and shown in white. The flux of the third component diminishes the size of the photocenter semimajor axis but does not contribute to the astrometric signal due to its very long period. The photocenter semimajor axis would be larger and would more closely follow the yellow star if not for the third component.

opposite signs. These impostors may be identified as double-lined binaries (SB2) rather than exoplanets with a single observation, if the RV separation of the two stars is of the order of (or larger than) the combined absorption line width of the stars, and if the spectral resolution is sufficient. In that case, their identification as false-positive candidates is trivial.

However, depending on the spectral resolution of the instrument, the orbital phase of the observations, the orbital inclination, the period, the masses of the components, and the absorption line widths, each star's absorption lines may not always be clearly separated. When that is the case, the RV shift of the two sets of absorption lines may be identified as a change of the line width, i.e., the FWHM, of the combined line. Observing a small RV semiamplitude of what appears to be a line of a single star does therefore not rule out the possibility that the companion is an identical stellar twin. The midpoint of this combined line from two unresolved sets of absorption lines will RV shift slightly, given by small flux and/or rotation speed differences of the two stars. We simulated the RV shift of a combined line from two almost identical twin binaries to test whether its small RV semiamplitude could mimic that of a star orbited by a planetary companion.

Figure 4 illustrates this. Here, we assumed a simple $\epsilon = q^4$ mass–luminosity relation; though, as long as the mass ratio is always closer to 1 than the flux ratio, the steepness of the relation did not qualitatively change our results. We then varied the ϵ/q ratios of the simulated systems from 0 to 1 and calculated the mass of the companion as inferred by the astrometric method and the RV method; see the left panel of Figure 4. The width of the simulated absorption lines of the primary and secondary components was kept equal. In the right panel, we show that, as long as the RV semiamplitude is $\lesssim v \sin i$ of the components, the determined companion mass as determined by the two methods is very similar. However, the ratio of the RV-determined mass to the astrometric mass, $M_{2,\mathrm{RV}}/M_{2,\mathrm{astrometry}}$, becomes increasingly sensitive to small changes in rotation speed differences between the components and in the mass ratio of the components as ϵ/q approaches 1. In

conclusion, if the spectral resolution is low, both the astrometric and RV data may falsely—but consistently between the data sets—indicate the presence of an orbiting exoplanet for some systems. In those cases, changes in the line width will be a better indicator for identifying the stellar nature of the companion.

The Gaia spectral line broadening parameter vbroad, which is the median of epoch vbroad measurements from the Gaia Radial Velocity Spectrometer, may be useful for identifying twin binary systems without the need for ground-based follow-up. The median vbroad of the 412 Gaia non-single-star solutions with flux ratios above 0.25 is 15.9 km s^{-1}, whereas it is 10.9 km s^{-1} for the 19,799 systems with flux ratios below 0.25. Unfortunately, vbroad is only available for stars brighter than $G_{\mathrm{mag}}12$, and most current astrometric exoplanet candidates are found around fainter stars (see Figure 2).

4. Example Systems

In this section, we analyze spectra of six astrometric exoplanet candidate systems to clarify the nature of the companions that cause a Keplarian motion of their host star. The first three systems, HD 68638, HD 40503, and HIP 66074, also highlighted by Holl et al. (2022a), have publicly available archival high-resolution spectra that we reanalyzed. The latter three systems, Gaia DR3 2052469973468984192, Gaia DR3 1916454200349735680, and Gaia DR3 5122670101678217728, were investigated using high-resolution spectra that we obtained with the FIES spectrograph installed at the NOT. The RVs inferred from these spectra enable us to supply the nondegenerate orbital solutions for the photocenters of the former three systems. Below, we discuss our findings for each system separately.

4.1. HD 68638

HD 68638 (Gaia DR3 1035000055055287680) is a G magnitude 7.3 system whose orbital solution was highlighted in Holl et al. (2022a), Gaia Collaboration et al. (2022b) because of
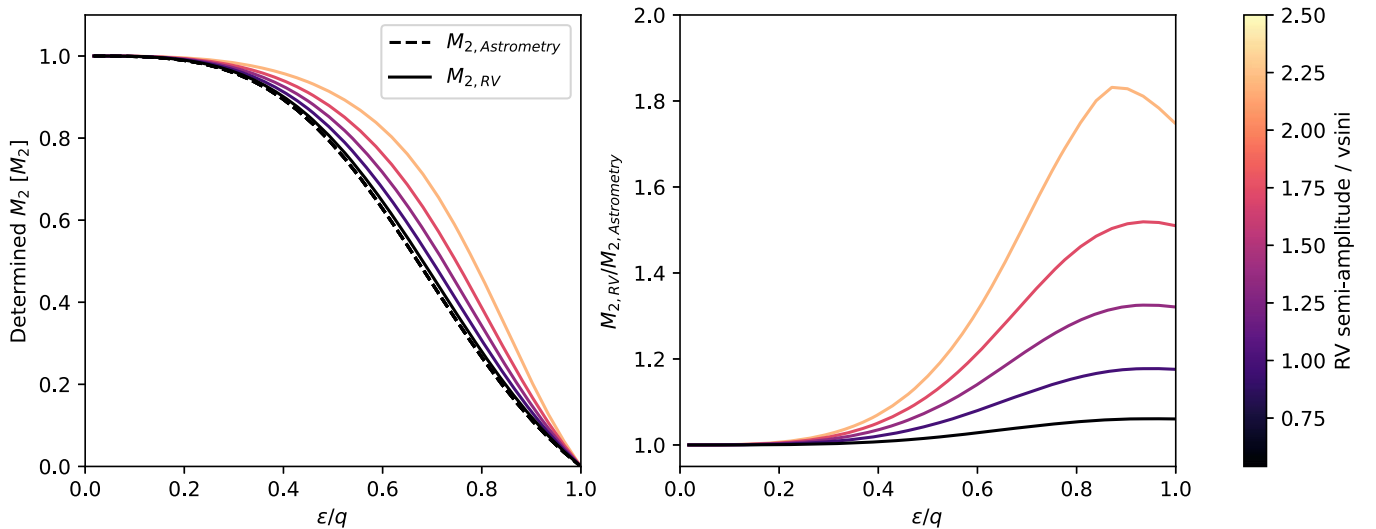
Figure 4. Astrometry and RV simulations. Left: the mass of a companion as determined by astrometry (dashed line) and RVs (solid lines) relative to its actual mass as a function of the flux ratio divided by the mass ratio, $\epsilon/q = (F_2/F_1)/(M_2/M_1)$. The line colors indicate the ratio of the RV semiamplitude to the absorption line widths, $v \sin i$. Right: the ratio of the RV-determined mass to the astrometry-determined mass.

its small photocenter semimajor axis. Despite its slightly elevated position in the H-R diagram (Figure 1), its Gaia DR3 lower bound flux ratio is 0. Although this system has previously been characterized as a binary system (Busà et al. 2007), in order to test our methodology and to better understand the characteristics of false positives, we reanalyzed the 27 publicly available ELODIE spectra of this system. In the bottom left panel of Figure 5, we present the cross-correlation functions (CCFs) obtained from these spectra along with the Gaia astrometric two-body orbital solution in the top left panel. Where the relative RVs are largest, the CCF displays two peaks with similar widths and heights, confirming the twin SB2 status of this system. The same conclusion was reached by Holl et al. (2022a), Gaia Collaboration et al. (2022b). In the top right panel of the same figure, we show the RV curve implied by the Gaia astrometric solution. To illustrate how the FWHM correlates with orbital phase, we show in the middle right panel the expected FWHM of the average absorption line as implied by the Gaia orbit. The measured FWHM of the ELODIE spectra are superimposed on this. By increasing the eccentricity of the Gaia orbit (shown as a dashed line) from 0.32 to 0.6, we get a better fitting orbit solution with the observed FWHM. For the sake of consistency, we calculated the FWHM of the total CCF even when the CCF splitting is apparent.

4.2. HD 40503

HD 40503 (Gaia DR3 2884087104955208064, HIP 28193) was discussed in Holl et al. (2022a), Gaia Collaboration et al. (2022b) as a potential new exoplanet discovery, because the 826 days orbital period derived by Gaia is consistent with the periodicity in publicly available Coralie and HARPS spectra. In Figure 6, we show CCFs from these spectra as well as the FWHM as a function of orbital phase, none of which indicate binarity. Because we see no indications that the companion is a binary, we compare the Gaia RV curve to the HARPS and CORALIE data points (top and right panels of Figure 6). Although we also find the Gaia period of 826 ± 50 days to be consistent within 2σ of our 758 days best fit to the RV data, the RV semiamplitudes are highly inconsistent: The Gaia

photocenter semimajor axis of $a_0 = 0.010$ au (0.25 mas) implies a companion mass of $5.18 \pm 0.59 \, M_{\rm Jup}$, assuming $F_2 = 0$, whereas the observed RV amplitude would imply a companion mass of $1.55 \pm 0.18 \, M_{\rm Jup}$. The observed discrepancies are possibly due to stellar activity affecting the RVs as noted by Holl et al. (2022a), Winn (2022). However, it is interesting that the ground-based RVs of HIP 66074 (see also below) as well as HR 810 (Winn 2022) also have much smaller RV semiamplitudes than their Gaia orbit counterparts.

4.3. HIP 66074

The system HIP 66074 (Gaia DR3 1712614124767394816) was discussed by Holl et al. (2022a), Winn (2022) because of its small photocenter semimajor axis of 0.0075 au (0.21 mas), which is consistent with a $6.9 \pm 1.1 \, M_{\rm Jup}$ mass companion. In Figure 7, we show our CCFs derived from the public High Resolution Echelle Spectrometer (HIRES) spectra that show no sign of double lines or FWHM changing with orbital phase, ruling out a twin binary system.

The orbital period, eccentricity, time of periastron passage, and argument of periastron from the Gaia orbital solution and the best RV fit to the ground-based data are all within just 1σ of each other (Winn 2022). However, there is an enormous factor 15 semiamplitude discrepancy between the ground-based RV data and Gaia astrometric data as highlighted by Holl et al. (2022a), Winn (2022). Interestingly, although they caution its interpretation, Winn (2022) do find an excellent fit between the two data sets with the only caveat that the companion needs a substantial flux ratio of $\epsilon = 1\% \pm 0.12\%$. This flux ratio is well above the mass ratio of $q = 0.063\%$, which would imply that the photocenter orbit is a scaled-down version of the companion's orbit and not the host star's orbit. It also implies a seemingly unrealistic luminosity of the planet: assuming the companion has a radius of $1 R_{\rm Jup}$, radiating 1% of the flux seen from HIP 66074 as a blackbody puts its effective temperature at around 3400 K! To find more plausible explanations to the large semiamplitude discrepancy, we considered several hypotheses. Below, we go through these and discuss the challenges each has:
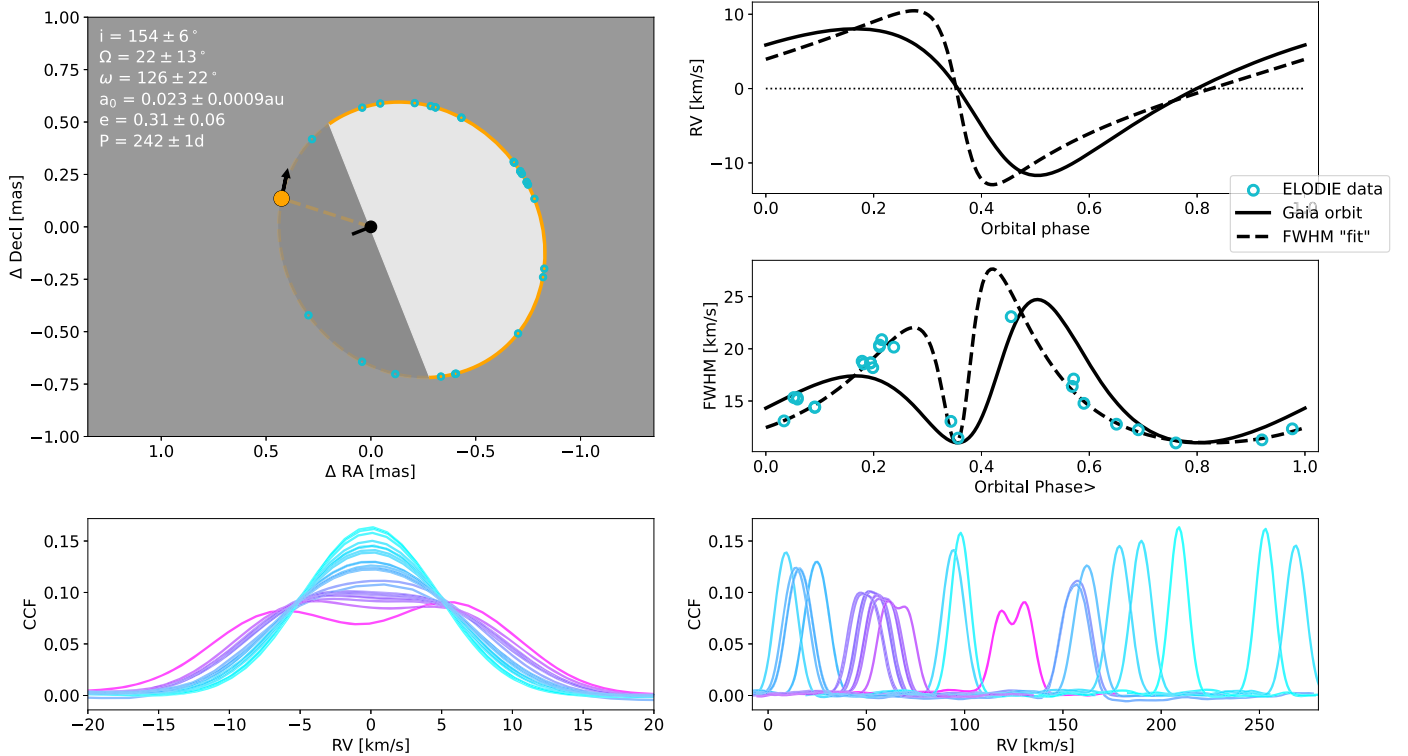
Figure 5. HD 68638. Top left: the geometry of the Gaia two-body orbital solution for the photocenter is shown with north pointing up and east pointing left. The Gaia parameters are printed as well. The barycenter is shown as a black dot, and the star is shown at periastron as an orange dot with the direction of motion indicated by the black arrow. The line through the barycenter represents the orbital angular momentum vector. The positive direction of the angular momentum is marked with an arrow that is occluded by the orbital disk in this particular view. The light gray part of the orbit with a solid orange outline indicates the near side of the sky-plane, and the dark gray part with a dashed outline indicates the far side of the sky-plane. The blue circles are the location on the orbit of the RV measurements. Bottom left: CCFs from all 27 publicly available ELODIE spectra are shown and colored according to their FWHM. Top right: the solid black line indicates the expected radial-velocity curve of the primary component based on the Gaia-derived orbital and stellar parameters assuming two equal-mass companions. The dashed line represents an orbit with a higher eccentricity of 0.6. Middle right: the FWHM of the CCFs is shown as blue dots as a function of orbital phase. The solid black line is the FWHM as a function of orbital phase inferred from the Gaia orbit. The dashed black line represents the FWHM of a more eccentric orbit that is a better fit to the observed FWHM. Bottom right: CCFs plotted with a horizontal offset, so their midpoints are located under their respective FWHM data points of the middle right panel.

There is no companion. The independent detections of an orbit with similar orbital parameters by Gaia astrometry and HIRES RVs make it very unlikely that the Keplarian motion of the source is a simple case of a false-positive detection.

Stellar activity affecting the RVs. Perhaps, as may be the case for HD 40503, stellar activity affects and mutes the RVs. If that were the case, we would not expect the RV semiamplitude to be the only affected parameter. We might also expect deformations in the CCFs, which we do not see (Figure 7).

Additional planets. This would affect the reflex motion of the host star and thus the RVs and could erase or mute a two-body orbital signal. However, because the astrometric and RV data would be affected equally by additional planets, it does not describe the large observed RV semiamplitude difference. Additionally, if the motion of the host star is the linear combination of several Keplarian orbits, the simple two-body model would not fit the data as well as it does.

The Gaia semimajor axis is overestimated. If the actual size of a_0 was a factor 15 smaller than the reported value of 0.21 ± 0.03 mas, then the two independent data sets would agree. The issue with this explanation is that an astrometric two-body orbit with an angular diameter of 0.014 mas would then have been detected, which is well below the precision of Gaia.

Triple system. Another potential explanation is that we are observing the orbit of a binary system, which itself is part of

a hierarchical triple system (Figure 3, right panel). In such a system, the astrometric and RV signature of the binary orbit could be muted by different amounts, preserving all observed characteristics of the orbit other than their apparent amplitudes. The mechanism is as follows: The hypothetical spectrum from such a system would be a combination of lines from all three components, but only the spectra from the two binaries would shift in velocity space. If the components are not separately identified in the spectrum, the obtained RV signal would be muted relative to a signal from just the binary system. The astrometric signal of the close binary would also be muted by the polluting light from the third component, but not necessarily by the same amount as the RV signal. As shown in Section 2, the astrometric signal is muted by a factor $(F_1 + F_2)/F_3$ by a bright third component on a long orbit.

The boundary conditions of this scenario are (i) the third component must be on a distant enough orbit that the corrections to the two-body orbit of the double-stars are undetectable, and (ii) it is close enough to the binary system that it cannot be spatially resolved by Gaia. To get an estimate of the possible range of orbital periods where both of these criteria are fulfilled, we conservatively assume a total mass of the triple system equal to the `binary_masses` m_1 mass. This puts an upper limit on the orbital period of the third component's orbit of around 16.5 yr. To calculate this, we
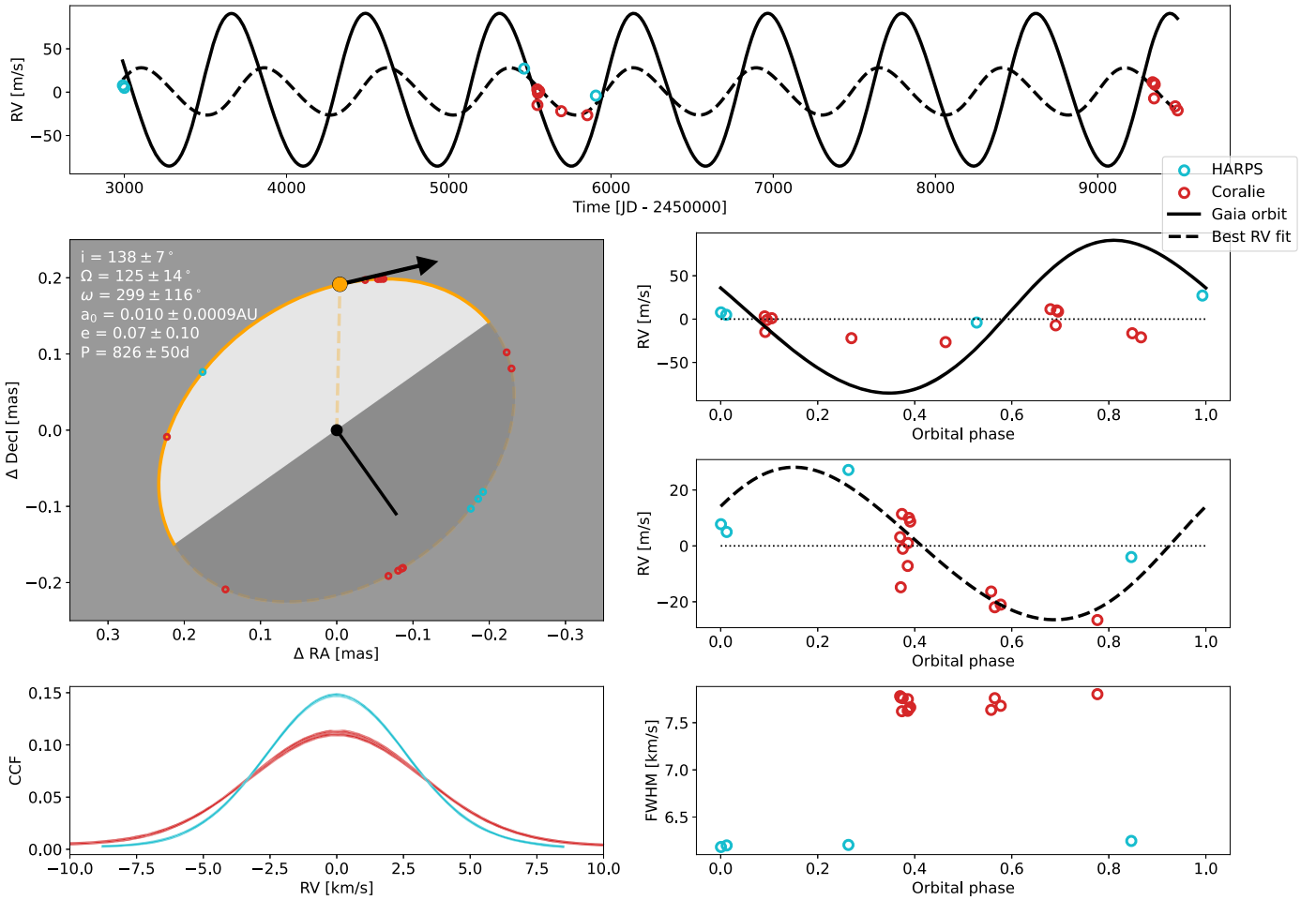
Figure 6. HD 40503. Shown here are the geometry and orbital parameters of HD 40503 as well as RV measurements in red and blue from the HARPS and CORALIE spectrographs respectively. The black dashed line represents the best fit to the RV data alone.

used its distance to us of 35 pc and Gaia's 0″23 two-body resolving limit.[3] On the near-end, the orbital period would need to be several times the 34 month baseline of DR3 to not significantly impact the two-body orbital solution. However, any unresolved companion with an intermediate orbital period (∼4–75 y; Gaia Collaboration et al. 2022b; Kervella et al. 2022) can also be probed by the difference in proper motion it will have caused between Gaia and HIPPARCOS single-source proper motions. The proper-motion anomaly between these catalogs for HIP 66074 is only $\chi^2 = 0.072$, where, for reference, a 3σ difference corresponds to $\chi^2 = 11.8$, leaving little room to hide for a third component. Even so, to test the scenario, we extended our simulation of RV and astrometric measurements of binary systems, described in Section 3, to encompass a third component. We also allowed the color, rotation speed, and flux ratio of the components to vary significantly. Lastly, we took into account the slightly redder bandpass of the Gaia compared to HIRES. Depending on the configuration of stars, the bandpass differences can amplify the relative brightness and thus the astrometric signal of two red binary stars relative to a hotter and bluer third component by as much as a factor ∼1.9. The effects on RVs by the inclusion of a third component in the spectrum depends on not only the flux ratios of the components but also the widths of the absorption

lines. A faster (slower) rotation of the third star compared to the two close components diminishes (increases) the impact of the third star on the combined spectrum, and thereby on the extracted RVs from that spectrum. The exact influence is further modified by the ratio of the rotational to orbital velocities at the epoch of observations and the RV extraction method, e.g., template matching, CCF, or the iodine method. Our simulations showed RV signals diminished up to ∼5–6 times (1.9 from the bandpass and ∼2.5–3 from differences in flux and rotation) relative to the astrometric one, but none of the configurations we tested were able to reproduce all the observables to a satisfying degree.

Additionally, our simulations showed that the RVs were muted in an increasingly nonlinear fashion as the influence of the third component increased. The resulting deformed shape of the RV curve meant worse fitting RVs at best and an unrecognizable RV curve at worst. We note that the HIRES observations employed the iodine method (e.g., Butler et al. 1996), and we tested here the effect of the third star on the CCFs and its RVs as measured by a Gaussian. We do not expect the effect of the third star on the HIRES RVs to be exactly the same.

Nearly face-on orbit. An *easy* way to get a large difference in semiamplitude between the astrometric and RV orbits is if the orbit of HIP 66074 is seen nearly face-on rather than edge-on. The orbital inclination of $i = 90°3 \pm 4°67$, as reported in Gaia DR3, does make this explanation seem unlikely. However, the
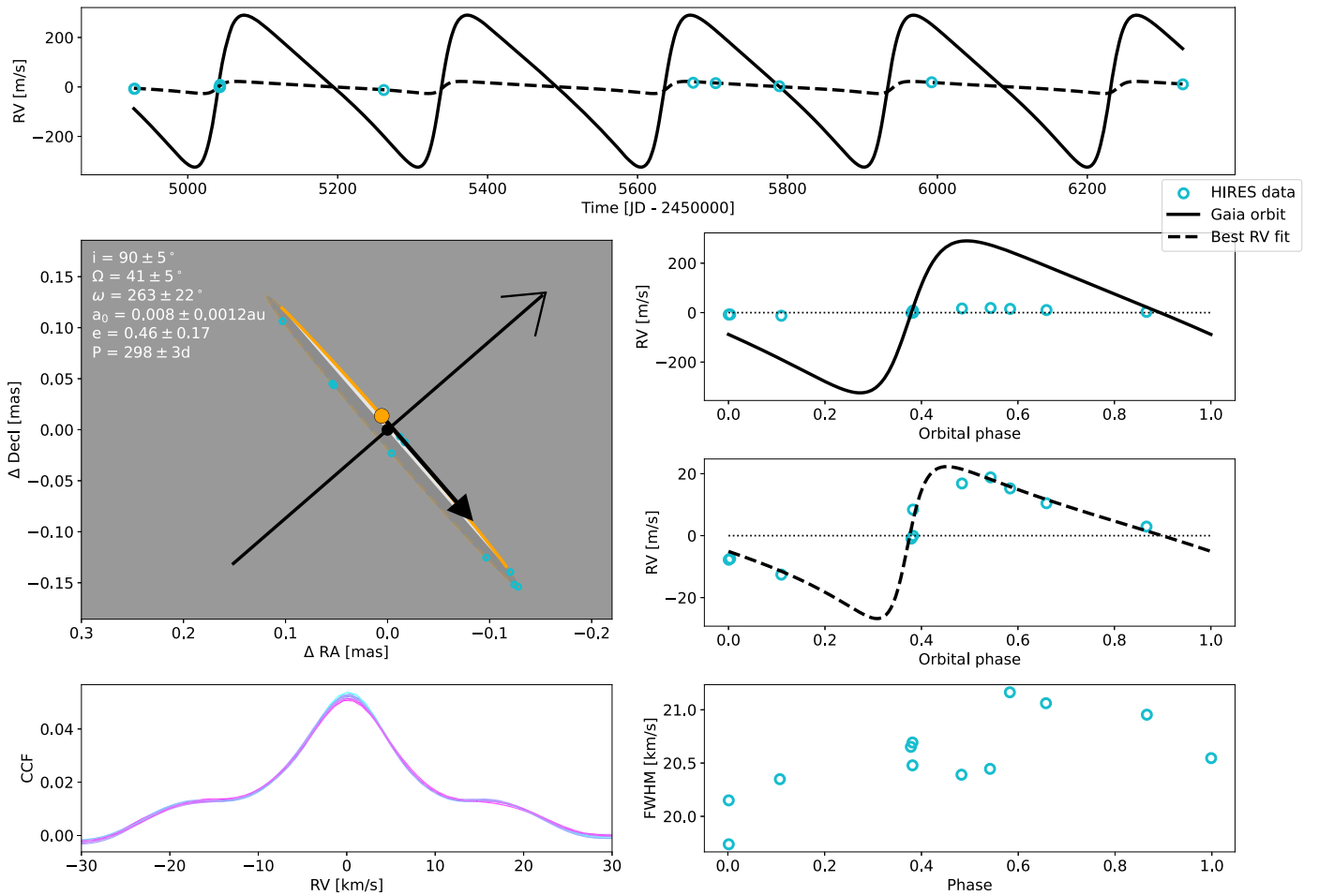

Figure 7. HIP 66074. Shown here are the Gaia geometry and orbital parameters of HIP 66074 as well as RV measurements in blue derived from HIRES spectra. The Gaia astrometry and RV data are in excellent agreement except for a large factor 15 disagreement in the RV amplitudes between the data sets. In the bottom left, we show CCFs that we obtained from the HIRES spectra. In contrast to Figure 5, the CCFs from the different observations are so similar that they look like one, ruling a stellar companion.

one-dimensionality of the Gaia along-scan abscissa measurements for targets dimmer than $G = 13$ can give rise to degenerate solutions of the two-body models that are not necessarily close in parameter-space (Holl et al. 2022b). It may also be worth noting that the majority of exoplanet candidates lie above this exact magnitude threshold. The issue will be more prominent if the number of data points is not much larger than the number of free parameters of the model. As mentioned in Section 1, the Gaia `nss_two_body_orbit` solutions have 12 free parameters. In the case of HIP 66074, 38 measurements spread out over 28 distinct visibility periods[4] were used to calculate the astrometric solution. 28 visibility periods is in fact higher than the exoplanet candidate average, giving no obvious reason to distrust the quoted orbital inclination. Without access to the epoch data, a more in-depth analysis is not currently possible.

4.4. Gaia DR3 1916454200349735680

Gaia DR3 1916454200349735680 (G5680) is the first of three systems we observed with the FIES spectrograph at the NOT. We obtained two spectra of the system three weeks apart. G5680 is characterized in Gaia as a K-dwarf and has a G magnitude of 10.9. Its location in the H-R diagram is visibly elevated; see Figure 1. This elevation was the reason for including it in our small sample as it serves as a test of whether the location in an H-R diagram can be used to gauge the likelihood of a binary false positive. The suspicion that this system was a binary was confirmed right away by inspecting the CCFs (Figure 8, top panel). The CCF of both spectra displays a clear double peak structure indicating it is an SB2. The similar heights and widths of the CCFs show that the two stars are very similar and that this system is a prototypical twin binary impostor. The difference in the separation between the CCF peaks implies a decrease in the radial component of the primary component's orbital velocity from ~ 7.7 to $\sim 5.8\,\mathrm{km\,s^{-1}}$ in the 21 days between our observations of the system. Such a decrease in RV fits with the first observation being at an orbital phase of around 0.92 and the second at 1, corresponding to 18.3 days. Here, we assumed equal mass of the components equal to the M_1 `binary_masses` value of $0.63 M_\odot$ and using Gaia's orbital inclination of $127°$. The period and inclination of the `nss_two_body_orbit` orbital solution are thus consistent with our observations.

---

[4] A visibility period is defined as "a group of observations separated from other groups by a gap of at least 4 days" as paraphrased from the Gaia online documentation, https://gea.esac.esa.int/archive/documentation/GDR3/.
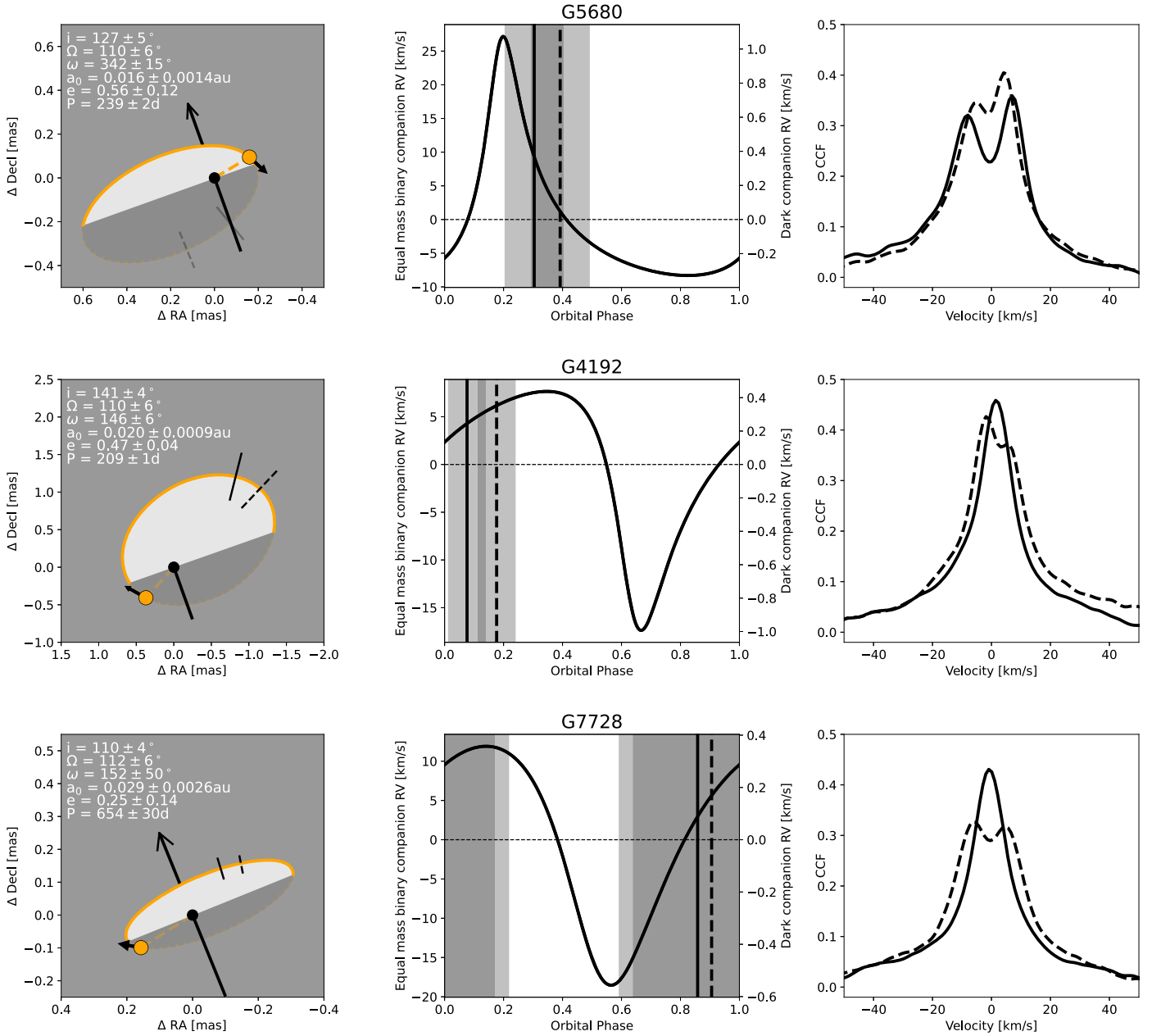
Figure 8. NOT targets. Each row corresponds to one of the three NOT fast-track targets. These systems are, from top to bottom: Gaia DR3 052469973468984192, Gaia DR3 916454200349735680, and Gaia DR3 5122670101678217728. Left column: the most likely orbits from the Gaia astrometric two-body solution are shown alongside the orbital parameters and their uncertainties. Middle column: RV curve of the primary component as inferred from the Gaia orbital solution. The left *y*-axis scaling assumes the companion to have a mass equal to the primary. The right *y*-axis scaling assumes the companion to be dark. The two NOT observations are shown as solid and dotted lines. The gray shaded areas indicate the 1σ uncertainties in orbital phase of these observations. The rectangles are darker where the uncertainties overlap. The large uncertainties in orbital phase timing are caused by the long baseline between the Gaia and NOT observations. Right column: CCFs obtained from the FIES spectra, using line styles corresponding to those from the middle column.

4.5. Gaia DR3 2052469973468984192

Gaia DR3 2052469973468984192 (G4192), our second FIES target, is classified as an M-dwarf with a *G* magnitude of 10.7. It is located right on the single star main sequence in the H-R diagram (Figure 1), so the expectation would be that the small astrometric motion of the photocenter, $a_0 = 0.02$ au (1.14 mas), would originate from an orbiting brown dwarf with a mass of $22.9 \pm 1.6 M_{\rm Jup}$, as per Equation (3). However, despite the first observation showing only a single CCF peak, this system is also a twin binary system, evident by the two-peaked CCF of the second observation obtained a few weeks

later; see Figure 8 middle panel. The separation between the CCF peaks increases from 0 to 4.6 km s^{-1} between the two observations. Using the quoted inclination of 141° and $M_1 = M_2 = 0.47 M_\odot$, where the mass once again taken to be the `binary_masses` M_1 mass, this RV separation would be expected to take 33.2 days. The actual gap between the observations was 21 days. While not wildly different, we do not attempt to investigate whether this discrepancy is caused by an underestimate of M_1 or an overestimate of either the inclination or the orbital period. We do note however that $1/\sin 141° \approx 33.2/21$, or in other words, if the configuration

of the orbit is edge-on, it would exactly account for the discrepancy.

4.6. DR3 5122670101678217728

The third and last of our FIES fast-track targets is the system Gaia DR3 5122670101678217728 (G7728). It is classified as a *G*-dwarf by Gaia and has a *G* magnitude of 8.9. The observed photocenter semimajor axis is $a_0 = 0.029$ au (0.28 ± 0.03 mas), which amounts to a companion mass of $15.6 \pm 1.7 M_{\rm Jup}$, assuming the companion is dark and using the mass estimate of the primary provided by Gaia. However, just like the two other FIES systems, the binary nature of the system is revealed by the double peak feature of the CCF obtained at a larger RV separation; see the bottom panel of Figure 8. The two peaks are extremely similar in height and width indicating that this system hosts two twin stars and not a star and a planet. The separation between the CCF peaks corresponds to an RV increase of the primary of $6.4 \, {\rm km \, s^{-1}}$ over the 31 day period between our observations of this target. Using the same equal-mass assumption as the other systems, and using $M_1 = 1.04 M_\odot$, and $i = 110°$, corresponds to a 32.7 day gap starting from an orbital phase of 0.4. Our observations are thus consistent with the orbital solution of this system.

5. Conclusion

With 9 of the 72 astrometric exoplanet candidates being previously confirmed exoplanets, Gaia's ability to detect photocenter movements small enough to find exoplanets is validated by DR3 and shows the current and future impact of the Gaia spacecraft on exoplanetary science. In this work, we investigated the nature of six of these candidate systems using information contained in archival and newly obtained high-resolution spectra. We found four systems, HD 68638, Gaia DR3 1916454200349735680, Gaia DR3 2052469973468984192, and Gaia DR3 5122670101678217728, to be false positives. The double-peaked CCFs of these systems show that they all consist of two nearly equal flux binaries. In the remaining two systems, HD 40503 and HIP 66074, the candidates are possibly exoplanets, although inconsistencies between the RV and astrometric solutions exist. The astrometric solutions imply in both cases an RV signal significantly larger than that observed. Yet, all other orbital parameters are fully consistent between RV and astrometry. It is not clear what causes this, but a more face-on geometry of the orbits than that implied by the astrometric solution could solve the disagreements.

We found 30 systems in the Gaia two-body orbital solutions with photocenter semimajor axes small enough to indicate a star–planet system that were not among the released exoplanet candidates. These systems are likely binary stars as per Gaia's flux ratio estimates; see Figure 1. These 30 systems along with the four false-positive exoplanets discussed in this paper highlight the difficulties of detecting exoplanets using astrometry. In this work, we emphasize the need for spectra of high spectral resolution to supplement the astrometric data in order to reveal impostors by their double-lined nature or by the correlation of the FWHM with orbital phase. The high resolution is needed because the total wavelength shift of two sets of unresolved absorption lines from a binary system is

dimmed in almost perfect proportion to the astrometric dimming, imitating an exoplanet signal in both data sets. The silver lining of the twin binaries issue is the fact that the similarity of the components makes it easier to identify the splitting in two of the absorption lines because the absorption lines have similar depths.

ORCID iDs

Marcus L. Marcussen ⓘ https://orcid.org/0000-0003-2173-0689
Simon H. Albrecht ⓘ https://orcid.org/0000-0003-1762-8235

References

Arriagada, P., Butler, R. P., Minniti, D., et al. 2010, ApJ, 711, 1229
Bonavita, M., Gratton, R., Desidera, S., et al. 2022, A&A, 663, A144
Busà, I., Aznar Cuadrado, R., Terranegra, L., Andretta, V., & Gomez, M. T. 2007, A&A, 466, 1089
Butler, R. P., Marcy, G. W., Williams, E., et al. 1996, PASP, 108, 500
Butler, R. P., Vogt, S. S., Laughlin, G., et al. 2017, AJ, 153, 208
Curiel, S., Ortiz-León, G. N., Mioduszewski, A. J., & Sanchez-Bermudez, J. 2022, AJ, 164, 93
da Silva, R., Udry, S., Bouchy, F., et al. 2007, A&A, 473, 323
Gaia Collaboration, Arenou, F., Babusiaux, C., et al. 2022b, arXiv:2206.05595
Gaia Collaboration, Prusti, T., de Bruijne, J. H. J., et al. 2016, A&A, 595, A1
Gaia Collaboration, Vallenari, A., Brown, A. G. A., et al. 2022a, arXiv:2208.00211
Halbwachs, J. L. 2009, MNRAS, 394, 1075
Halbwachs, J.-L., Pourbaix, D., Arenou, F., et al. 2022, arXiv:2206.05726
Holl, B., Fabricius, C., Portell, J., et al. 2022b, arXiv:2212.11971
Holl, B, Sozzetti, A, Sahlmann, J, et al. 2022a, arXiv:2206.05439
Kürster, M., Endl, M., Els, S., et al. 2000, A&A, 353, L33
Kervella, P, Arenou, F, & Thevenin, F 2022, A&A, 657, A7
Marcy, G. W., Butler, R. P., Fischer, D., et al. 2001, ApJ, 556, 296
Mayor, M., Udry, S., Naef, D., et al. 2004, A&A, 415, 391
Minniti, D., Butler, R. P., López-Morales, M., et al. 2009, ApJ, 693, 1424
Moutou, C., Mayor, M., Lo Curto, G., et al. 2009, A&A, 496, 513
Naef, D., Mayor, M., Pepe, F., et al. 2001, A&A, 375, 205
Perryman, M., Hartman, J., Bakos, G. A., & Lindegren, L. 2014, ApJ, 797, 14
Sozzetti, A., Udry, S., Zucker, S., et al. 2006, A&A, 449, 417
Trifonov, T., Tal-Or, L., Zechmeister, M., et al. 2020, A&A, 636, A74
Winn, J. N. 2022, AJ, 164, 196
Wittenmyer, R. A., Horner, J., Tuomi, M., et al. 2012, ApJ, 753, 169